Journal of Magnetic Resonance 299 (2019) 135–150

Contents lists available at ScienceDirect

Journal of Magnetic Resonance

journal homepage: www.elsevier.com/locate/jmr

The twisted solenoid RF phase gradient transmit coil for TRASE imaging

Hongwei Sun, Stephanie Yong, Jonathan C. Sharp *

Department of Oncology, University of Alberta, Edmonton, Alberta, Canada

ARTICLE INFO

Article history:
Received 4 July 2018
Revised 30 October 2018
Accepted 16 December 2018
Available online 17 December 2018

Keywords:
TRASE
RF coil
Phase gradient
k-space

ABSTRACT

TRASE is an MRI *k*-space encoding method that uses radio-frequency (RF or B_1) transmit phase gradient fields to achieve millimeter-level spatial resolution. Image quality is critically dependent upon the efficient generation of B_1 fields with uniform magnitude and strong phase gradients. We present the design of a new family of phase gradient transmit coil based upon a solenoid twisted about a transverse axis. This design has many attractive geometric, electrical and magnetic characteristics, including the capability to spatially encode in the direction of the main static B_0 field without obstructing access to the bore. Analytical, numerical simulation and experimental results are presented, including demonstration of 1-dimensional TRASE encoding without the use of PIN diode switches. Twisted solenoid coils significantly expand the capabilities of TRASE MRI.

1. Overview

TRASE (Transmit Array Spatial Encoding) is an MRI method that achieves *k*-space encoding by the use of gradients in the phase of the radio-frequency (RF) transmit fields, instead of gradients in the static (B_0) field. Clinical-level millimeter spatial resolution has been demonstrated in phantom studies [1–3]. Since TRASE allows the B_0 gradient encoding system to be replaced by simpler RF technology, TRASE is a promising technique for low-field, low-cost MRI systems [4]. These systems often employ permanent magnets with a transverse or vertical B_0 magnetic field. The TRASE pulse sequence consists of an echo train using 180° refocusing pulses, in which the phase gradient transmit field is switched between each RF pulse, in an alternating pattern. Since image quality is critically dependent upon the ability to efficiently generate these B_1 fields with uniform magnitude and strong phase gradients, there is an ongoing need for improved coil designs and the associated RF technologies. One limitation of current TRASE systems is that no practical transmit design for encoding along the B_0 direction for a transverse B_0 geometry has been proposed. Such a coil must generate a B_1^+ field vector whose direction varies along the transverse B_0 direction so as to create a linear phase slope along B_0 for spatial encoding. In a theoretical study Bellec et al. applied a target field design process for a G_y phase gradient for a transverse B_y directed B_0 field, resulting in a strong phase gradient, but limited $|B_1|$ homogeneity [5]. This work demonstrated that a phase gradient for this geometry is possible in principle, however the wire path design presented was incomplete and experimental results were not presented.

The first RF phase gradient coil used for TRASE was a twisted birdcage coil [1,6] modified with a twist about the axis in the B_0 direction. For a conventional superconducting magnet design, this corresponds to a twist along the patient superior-inferior axis. The spark for this work was to ask the question: "Is there an analogous twisted geometry for low field magnets, for which the B_0 direction is transverse?" The standard coil for low field systems is the solenoid, so this suggests a solenoid twisted about a transverse axis [7], which would retain all the desirable features that a solenoid coil possesses for a transverse B_0 field (high efficiency ($\mu T/A$), uniformity, large imaging field-of-view (FOV) relative to aperture, cylindrical geometry), while simultaneously generating a phase gradient along a transverse axis. The specific aims of this study are to explore the use of the twisted solenoid transmit RF coil in spatial encoding for a cylindrical coil geometry. We design and experimentally verify a twisted solenoid coil pattern, subject to the multiple constraints of maximizing efficiency, $|B_1|$ uniformity and phase gradient strength. Since the usable imaging volume is effectively defined by the $|B_1|$ uniformity, the FOV is not an independent design constraint. Similarly, phase gradient linearity was not enforced as a design constraint, since all designs provided acceptable linearity.

* Corresponding author.
E-mail address: jcsharp@ualberta.ca (J.C. Sharp).

https://doi.org/10.1016/j.jmr.2018.12.015
1090-7807/

1.1. TRASE encoding principles

Consider an RF transmit field with a spatially-dependent phase of $B_1 = |B_1|e^{i\phi(r)}$, of the specific form in which the phase varies linearly along a spatial axis of $\phi(r) = 2\pi\ k \cdot r = G \cdot r$. This RF phase gradient field can be represented in k-space as an off-center point k ('coil k-space origin') [1]. Refocusing with a 180° pulse using a phase gradient coil causes the spin state to be reflected about the coil k-space origin. The fundamental concept of TRASE spatial encoding is that k-space traversal is possible in an echo train sequence in which a series of 180° refocusing pulses with different RF phase gradient coils are used. TRASE imaging experiments therefore require a set of transmit coil configurations capable of providing a series of different B_1 phase gradients. A key motivation for developing TRASE technology is that high spatial resolution is attainable because signal phase accumulates down the echo train to reach high k-space states [1].

TRASE phase evolution occurs discretely at each refocusing pulse, with each echo represented a point in k-space, with higher k-space encoding corresponding to later echoes. For one-dimensional TRASE encoding, two fields A and B with a difference in phase gradient are needed. The basic 1D sequence consists of a 90° excitation pulse followed by a series of 180° refocusing pulses, applied alternately on the A and B coils. After each refocusing pulse, echo data are acquired at a k-space sample spacing of $\Delta k = 2|k_A - k_B|$, i.e. the spacing is determined by the difference of the coils' phase gradient strengths.

Since TRASE is an alternative way of encoding MRI data in k-space, all familiar k-space principles may be directly applied to TRASE [3]. The FOV without aliasing is given by the reciprocal of the k-space point spacing, whereas the spatial resolution (Δx) is proportional to the reciprocal of the sample k-space extent [8,9]. We can therefore write the following: FOV $= 1/(2|k_A - k_B|)$ and $\Delta x = 1/(2|k_A - k_B| \cdot ETL)$, where ETL represents echo train length. It follows that the achievable spatial resolution depends upon the practical length of the echo train.

TRASE image resolution is affected by k-space filtering caused by T_2 losses and other mechanisms (e.g. diffusion) causing signal loss down the echo train, since the later echoes correspond to the high spatial frequency information. A rule-of-thumb is that the duration of the echo train should be no longer than 1.2 times the shortest T_2 to be imaged [4,10]. Although a longer train may be used, the resolution of the shortest T_2 species will become T_2 limited, rather than sampling-limited. This T_2 constraint is the motivation for the implementation of echo trains consisting of short high-power RF pulses.

1.2. TRASE coil requirements

1.2.1. B_1 Phase gradient and pulse length

To illustrate the potential for clinical feasibility, consider the example of TRASE-encoded brain MRI, for the following parameters: matrix (ETL) = 128, FOV = 22.5 cm, pixel = 1.76 mm. In-plane encoding requires two opposed 4.0 deg/cm phase gradients, which is within the achievable range, (see Table 1). Note that for 2D imaging, 128 echo trains (of 128 echoes each) would be required, assuming full k-space sampling. Considering the shortest T_2 of 42 ms for white matter at 0.2T [4,11], the above rule-of-thumb requires the total echo train duration, $t_{TRAIN} < 1.2T_2 = 50.4$ ms, and an echo spacing of $1.2T_2/ETL = 394$ μs. Assuming a 50% duty cycle between transmit and receive, this equates to a 200 μs length for each refocusing pulse, which is within an achievable range, for example see Der [12]. In summary, clinically useful imaging becomes increasingly feasible for a combination of parameters such as gradients $\geqslant$ 4.0 deg/cm; pulses $\leqslant$ 200 μs; over imaging FOV of $\geqslant$ 20 cm. The coil development described here addresses all these parameters.

1.2.2. $|B_1|$ Homogeneity

There are $|B_1|$ homogeneity requirements for TRASE. We will only consider rectangular ('hard') refocusing pulses and image reconstruction by Fourier Transform (FFT), although other pulse designs [13] and other reconstruction techniques [14] may allow the $|B_1|$ homogeneity requirements outlined here to be relaxed. Since TRASE relies on the phase reversal behaviour of refocusing pulses for successful spatial encoding and minimization of image artifacts, the TRASE sequence requires effective refocusing behaviour over the imaging volume for each pulse in the pulse train. From previous work [3], this constrains the maximum $|B_1|$ coil inhomogeneity to be less than approximately ±10% to ±15%. For the purposes of this paper, we will adopt the more conservative figure of ±10%, which corresponds to a usable refocusing flip angle range of approximately 160–200°. Although a useful rule-of-thumb, there are many other factors that may affect the acceptable flip angle errors in refocusing for a particular coil. Some of these factors include off-resonance effects; the performance of other coils being used; tolerance of the imaging application to artifacts; the effectiveness of artifact removal processing; and details of the pulse sequence including pulse phases, and phase cycling schemes.

1.3. TRASE array configurations

There are a number of different possible transmit hardware configurations, as shown in Fig. 1. In Fig. 1A and B, two different configurations are shown for driving a Helmholtz-Maxwell (HM) pair. Both HM coil elements must be driven simultaneously to produce a phase gradient field. To allow the phase of the Maxwell coil to be reversed, it is necessary that the two elements be driven independently and so the coupling parameter S_{12} becomes important. A value of at least $S_{12} < -15$ dB, or preferably $S_{12} < -20$ dB is desirable to ensure effective decoupling. This level of decoupling is

Table 1
Comparative data for TRASE phase gradient systems. Although the twisted birdcage has favourable geometric and field performance, it is unusable with a transverse B_0 field. The Helmholtz - Maxwell (HM) coils, have the disadvantage of a large difference between the inner and outer diameters. Being rectangular, the HM design is better suited to parallel pole plate magnets than to cylindrical Halbach magnets. Stockmann's coil is a cylindrical Helmholtz - Maxwell concept, in which the cosine field is produced by a short multi-turn birdcage. This produces a gradient along the patient axis, so could be used to complement the transverse encoding offered by the twisted solenoid designs.

Geometry	Coil I.D. (cm)	Coil O.D. (cm)	Imaging Volume FOV x L (cm)	Phase Gradient G (deg/cm)	Gradient Direction(s)	Reported Pulse Len (t_p) (μs)	Encoding Efficiency ($2G/2t_p$) (deg/cm)/ms
Twisted Birdcage (Sharp, 2010)	9	9	2.5 × 2.5 × 14	12.5	∥ B_0 and SI	800	15.6
Helmholtz - Maxwell (Deng, 2013)	22	42	16 × 16 × 14	5	⊥ B_0 and SI ⊥ B_0 and LR	300	16.6
Helmholtz - Maxwell (Der, 2018)	22	42	16 × 16 × 14	5	⊥ B_0 and SI ⊥ B_0 and LR	130	38.5
Birdcage - Maxwell (Stockmann, 2016)	18	22	4 × 4 × 13	2.25	⊥ B_0 and SI	192	11.7

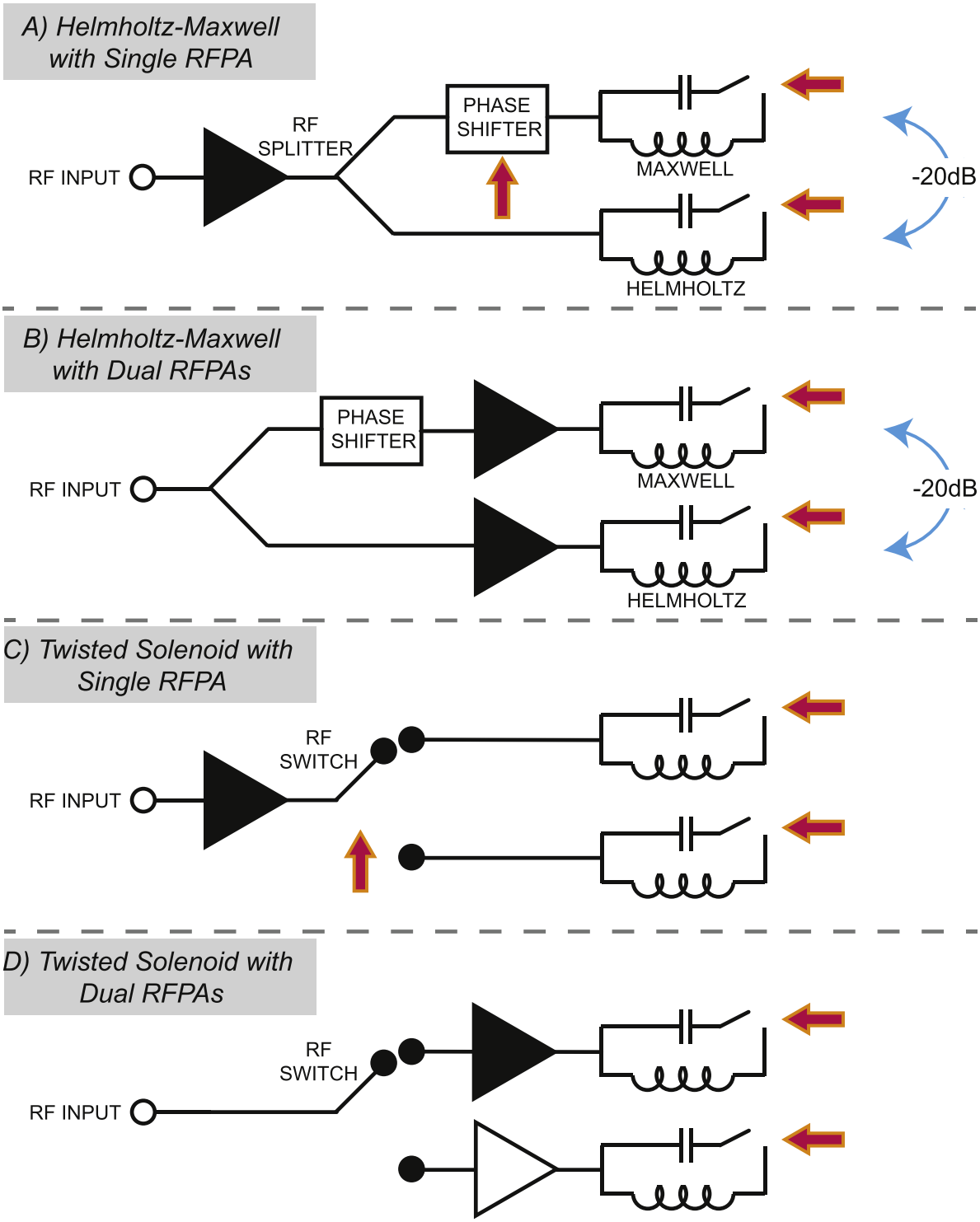

Fig. 1. Four possible TRASE transmit configurations for a single encoding axis. (A) Helmholtz-Maxwell pair using a single RF power amplifier (RFPA). (B) Helmholtz-Maxwell pair using dual RFPAs. Both of these configurations require good geometric decoupling, i.e. $S_{12} < -20$ dB. (C) A pair of twisted coils using a single RFPA. (D) A pair of twisted coils using dual RFPAs. Each configuration is shown with a single RF input, although configurations B and D could alternatively be driven by dual transmit channels. High power active elements (under PIN diode control) are shown with a red arrow. (For interpretation of the references to color in this figure legend, the reader is referred to the web version of this article.)

achievable, but requires rather delicate adjustments [2,4]. A significant advantage of twisted designs (shown in Fig.1C and Fig.1D is that the resonant elements are driven sequentially, so it is not necessary to geometrically decouple elements which are simultaneously enabled and tuned to the same frequency. For this reason, twisted pair designs are more robust to experimental perturbations than HM coils. In all configurations, active enable/disable has been shown, because for 2D encoding applications (with a total of 4 coils) this function is expected to be required.

Configuration *A* shows a single RF power amplifier (RFPA) with a power splitter and actively-controlled phase shifter, both located after the single amplifier [2]. This configuration has the

disadvantage that these additional RF components must operate under high power conditions. Deng et al. used configuration *A* including a high power RF splitter, a high power PIN diode phase shifter, and PIN diode coil element disable circuitry [2]. Configuration *B* alleviates the need for high power components, at the expense of a second amplifier, although this is mitigated because each individual amplifier has a lower peak power requirement, than in *A*. Configuration *B* uniquely allows some limited flexibility to adjust the gradient strength by adjustment of the relative drive levels, whereas configuration *A* has a fixed power ratio determined by the design of the high power RF splitter. Both configurations *A* and *B* demand a high duty cycle from the RFPA because both coils are active for generation of both positive and negative phase gradients.

Configurations *C* and *D* show respectively single and dual RFPA configurations for a pair of twisted coils. Configuration *C* requires a higher duty cycle and a high power switch, whereas *D* requires one RFPA for each coil. Of all the configurations, Configuration *D* has the lowest duty cycle requirement (indicated graphically by shaded the RFPA in standby in white), hence, *D* is used in this paper.

The various configurations have different characteristics when extended to 2-dimensional encoding. In *A*, if a single RFPA is maintained, then cascading of splitters and an additional switch is required. Configurations *B* and *D* require additional power amplifiers but are otherwise straightforward. Configuration *C* would require a 4-way high power RF switch.

1.4. Performance of phase gradient systems

A 'phase gradient system' comprises one or more RF power amplifiers (RFPAs) and an RF transmit array capable of producing phase gradient fields. For an RF coil *A* with *k*-space origin of k_A(1/m), the inherent B_1 phase gradient is $G_A = 2\pi k_A$ (rad/m). We will consider 1-dimensional encoding, which requires the production of two different RF transmit field patterns (*A* and *B*), both with (preferably) uniform B_1 field magnitude, but maximally different B_1 phase gradients. We will denote the phase gradient difference between the two fields as ΔG_{AB}.

The image FOV for a single-shot echo train using fields *A* and *B* is the reciprocal of the k-space sampling interval, i.e. $\mathrm{FOV} = 1/2|k_A - k_B| = 1/2\Delta k_{AB}$. The pixel separation ('pixel size') $\Delta x = \mathrm{FOV}/ETL$, where *ETL* is an integer 'echo train length' equal to the number of echoes. For example, for two phase gradient coils of strengths +5.0 deg/cm and −5.0 deg/cm and *ETL* = 128; we have Δk_{AB} = 10.0 deg/cm = (10/360)/0.01 = 2.78 cycles/meter. The pixel size is therefore:

$$\Delta x = \mathrm{FOV}/ETL = 1/(2 \times \Delta k_{AB} \times ETL) = 1/(2 \times 2.78 \times 128) = 1.41 \text{ mm}.$$

This raw resolution calculation shows that rather modest and achievable phase gradients are sufficient to attain clinical level spatial resolution, provided that a long echo train may be used. This is the motivation behind this research program aimed at developing the technology to perform these experiments.

A key performance parameter for a practical imaging system is the rate at which *k*-space encoding may be achieved. This '*k*-space trajectory speed' is analogous to the maximum gradient strength in a conventional B_0 gradient system. Consider a sub-section of a TRASE echo train consisting of two refocusing pulses of $(-\tau_A - \tau_B -)$, where τ denotes pulse duration. To quantify encoding performance we will define a 1-dimensional TRASE image encoding efficiency metric as follows: Encoding Efficiency $= \Delta G_{AB}/(\tau_A + \tau_B)$. The inter-pulse delay (for signal acquisition) has been omitted from this metric, as the selected value is not indicative of the transmit hardware encoding performance. In analogy with conventional B_0 gradient coils, gradient coil size is a major determinant of encoding efficiency. A larger phase gradient coil will have a lower encoding efficiency for two reasons. Firstly, the phase gradient strength scales inversely with coil linear dimensions, and secondly for a given available RF power, the pulse length will be longer (with details depending upon coil geometry). Higher available RF power will increase the encoding efficiency of the overall phase gradient system. Table 1 provides information collated from the literature on TRASE encoding systems.

2. Theory

2.1. Tilted and twisted solenoids

Solenoids can be tilted and paired to produce a uniform transverse magnetic field. For a superconducting DC application, Goodzeit et al. [15] proposed a two-element double helix dipole constructed from two tilted solenoid coils. By use of opposing currents their design cancels the longitudinal solenoidal component, to obtain a resultant dipole field. The field is uniform within the bore. These solenoids are tilted, but not twisted, so do not produce the phase gradient required for TRASE. Alonso has applied the same tilted double helix dipole field as an NMR RF coil [16].

Fortuitously, analytical fields for twisted solenoids of exactly the type we require for TRASE are to be found in the literature on magnet design [17,18] in the form of 'Modulated Double Helical Coils'. Just one of these coils is required to produce a field gradient for TRASE. Here we will present the first use of the twisted field pattern in an NMR RF coil, as an imaging gradient. Since our application is low-field imaging, the quasi-static (DC) analysis of the coil field pattern is applicable.

2.2. Ideal long twisted solenoid

In this section, we investigate how phase gradient strength and $|B_1|$ uniformity vary as a function of twist parameter, coil diameter and diameter of imaging volume. This will be based on the analytical solution for the infinite, closely wound twisted solenoid of Queval [18].

2.2.1. Wire path on cylindrical surface

We will consider coil geometries for which a wire wound on the surface of a cylinder lies on the parametric curve $P(\theta)$:

$$\begin{aligned} P_x(\theta) &= a\cos(\theta) \\ P_y(\theta) &= a\sin(\theta) \\ P_z(\theta) &= A\sin(n\theta + \psi) + (h/2\pi)\theta \end{aligned} \tag{1}$$

where the parameters are as follows (see Fig. 2):

- a (m) - coil turn radius (radius of cylindrical former)
- A (m) - twist or modulation amplitude, which controls the phase gradient strength. (For a uniform solenoid, $A = 0$.)
- n - coil multipole order. For TRASE purposes, this parameter is restricted to $n = 2$.
- ψ (radians) - winding shift. Note that a rotation of the TRASE coil former about the z axis by $\Delta\alpha$ is equivalent to a $2\Delta\alpha$ change of winding shift (see details in Section 2.2.4)
- h (m) - turn advance or pitch (Turns/meter = $1/h$)
- θ (rad) - cylindrical coordinate varying between $-N\pi$ and $N\pi$ (shown in Fig. 2), where N represents the number of coil turns

To illustrate, consider two examples. Firstly, a single circular planar loop of radius a is given by the curve $P(-\pi) \rightarrow P(\pi)$, for $A = 0, \psi = 0, h = 0$. Secondly, a 4-turn solenoid of turn radius a

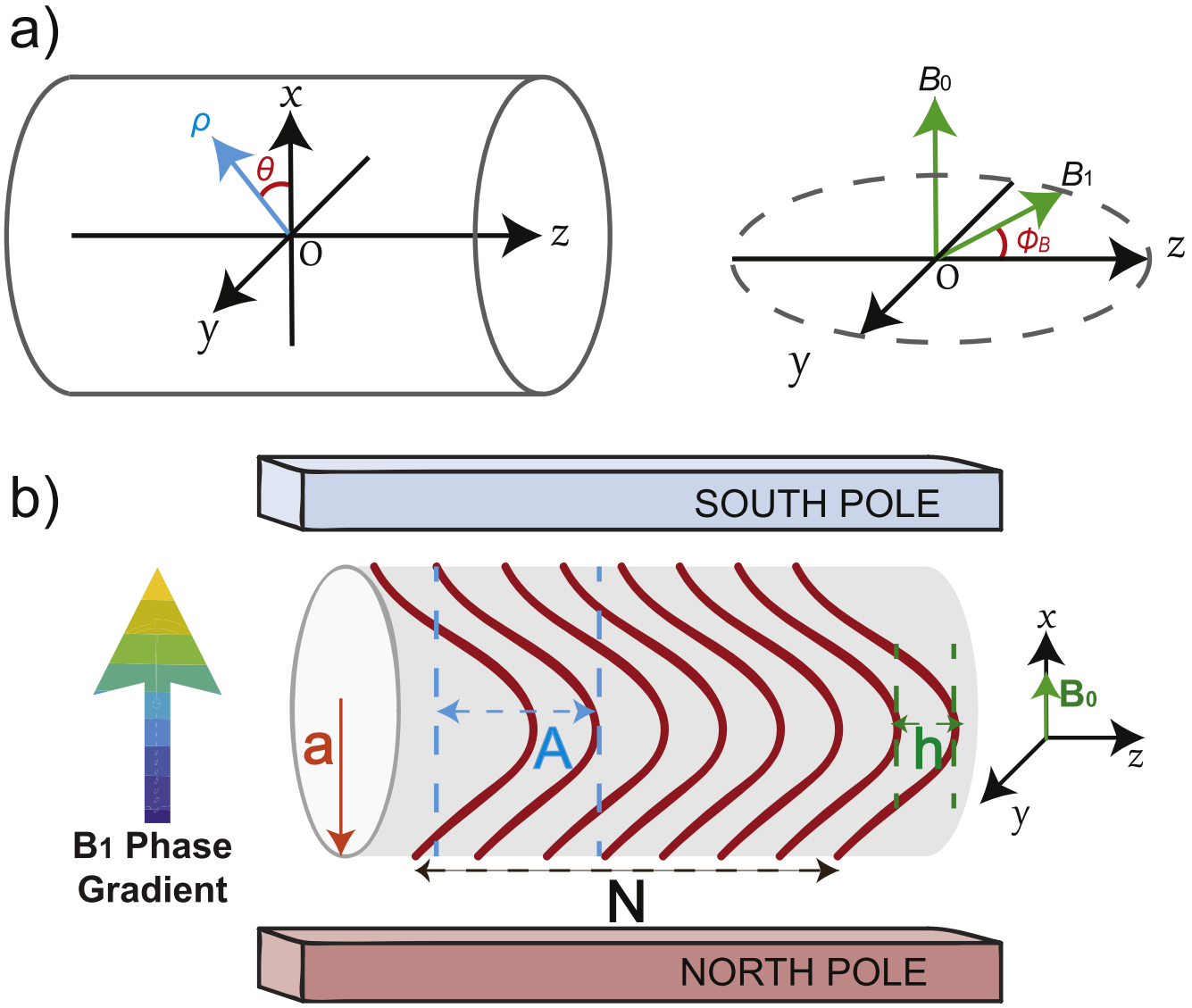

Fig. 2. (a) Cylindrical (ρ,θ,z) and Cartesian (x,y,z) coordinate systems, showing cylindrical coil former. The main magnetic field B_0 is applied vertically, that is along the x direction. The B_1 field is the RF field in the yz plane and has phase ϕ_B, which is x-dependent: $\phi_B(x)$; (b) A cartoon of a twisted solenoid coil positioned inside a magnet. The parameters that determine coil wire pattern are depicted.

and length L, is given by the curve $P(-4\pi) \rightarrow P(4\pi)$, for parameters $A = 0, \psi = 0, h = L/4$.

For the twisted solenoid designs in this paper we will fix $\psi = 0$ and $n = 2$. Other designs are obtained by simple rotation of the former or wire pattern. This condition of $\psi = 0$ corresponds to the wire axial offset $P_z(\theta)$ starting at zero for $\theta = 0$. We will refer to $\theta = 0$ as the 'top' of the coil, and this geometry will produce a phase gradient in the x, up-down direction. The maximum z (axial) offset of the wire occurs $2n$ = 4 times per turn, for values of θ satisfying $|\sin 2\theta| = 1$, i.e. $\theta = -3\pi/4, -\pi/4, \pi/4, 3\pi/4 \ldots$.

2.2.2. Magnetic field

To calculate the field within the cylindrical aperture due to a steady current in the wire, we will consider the continuous current sheet approximation, which is equivalent to a coil wound tightly with thin wire. Although the fields outside the aperture are non-zero, we will ignore these, as our concern is the imaging volume within. So for a thin wire, tightly wound coil of radius a and infinite length with its axis along the z–axis, current I, the B field components in cylindrical coordinates (ρ,θ,z), within the aperture $(\rho < a)$ are [18]:

$$\begin{aligned} B_\rho &= -\mu_0 \tfrac{I}{h} \tfrac{A\rho}{a^2} \sin(2\theta + \psi) \\ B_\theta &= -\mu_0 \tfrac{I}{h} \tfrac{A\rho}{a^2} \cos(2\theta + \psi) \\ B_z &= \mu_0 \tfrac{I}{h} \end{aligned} \tag{2}$$

B_ρ is the radial component, B_θ is the circumferential component, and B_z represents the axial component. We can define Cartesian coordinates $(x,y,z) = (\rho\cos\theta, \rho\sin\theta, z)$. Transforming these field components to Cartesian coordinates:

$$\begin{aligned} B_x &= -B_\theta \sin\theta + B_\rho \cos\theta \\ B_y &= +B_\theta \cos\theta + B_\rho \sin\theta \\ B_z &= \mu_0 \tfrac{I}{h} \end{aligned} \tag{3}$$

Notice that the B_z uniform solenoidal component is unaffected by the twist modulation.

2.2.3. NMR B_1 field

For our NMR purposes, we wish to use the twisted solenoid as a B_1 RF transmit coil. In what follows it is always useful to bear in mind that the direction of the B_1 *field itself* is in general distinct from the direction of the B_1 *phase gradient*. As for all RF coils, the coil itself produces an RF magnetic vector field with three components, but only the two components orthogonal to the main magnetic field B_0 contribute to the NMR B_1 field. We will restrict the discussion to the case of the static field B_0 applied in the x direction, which we set as the vertical direction. For this B_0 field direction, the contributing transverse B_1 components are B_y and B_z, while any B_x component becomes a concomitant RF field, i.e. does not contribute to B_1, hence, can be ignored in our discussion. The B_1 field components, magnitude $|B_1|$ and phase ϕ_B can be written as:

$$\begin{aligned} B_y &= +B_\theta \cos\theta + B_\rho \sin\theta \\ B_z &= \mu_0 \tfrac{I}{h} \\ |B_1| &= \sqrt{B_y^2 + B_z^2} \\ \phi_B &= \tan^{-1} \tfrac{-B_y}{B_z} \end{aligned} \tag{4}$$

For this definition of the phase, $\phi_B = 0$ over the central horizontal ($x = 0$) plane. Since for this infinite current sheet, none of the field components are a function of z, there is no possibility of an axial B_1 phase gradient, i.e. $G_z = 0$. We can however usefully define gradients in B_1 phase ϕ_B in both lateral (i.e. non-axial) directions:

$$G_x = \frac{\partial \phi_B}{\partial x}, \quad G_y = \frac{\partial \phi_B}{\partial y} \tag{5}$$

However, for our chosen coil rotational orientation ($\psi = 0$), the B_1 phase gradient is in the vertical x-direction only (parallel to B_0) because B_z is uniform and B_y only varies as a function of x. This can be shown as follows:

$$\begin{aligned} B_y &= +B_\theta \cos\theta + B_\rho \sin\theta \\ B_y &= -\mu_0 \tfrac{I}{h} \tfrac{A\rho}{a^2} [\cos(2\theta + \psi)\cos\theta + \sin(2\theta + \psi)\sin\theta] \end{aligned} \tag{6}$$

which, using trig identities, $x = \rho\cos\theta$, and $\psi = 0$, simplifies to:

$$B_y = -\mu_0 \frac{I}{h} \frac{A\rho}{a^2} \cos(\theta + \psi) = -\mu_0 \frac{I}{h} \frac{Ax}{a^2} \tag{7}$$

The ratio of the B_1 components is:

$$\frac{B_y}{B_z} = \left(\frac{-A\rho}{a^2}\right) \cos\theta = \frac{-Ax}{a^2} \tag{8}$$

and the B_1 phase is:

$$\phi_B = \tan^{-1} \frac{-B_y}{B_z} = \tan^{-1} \left(\frac{Ax}{a^2}\right) \tag{9}$$

Since the phase is a function of x only, we have $G_y = 0$, and for the phase gradient in the x-direction:

$$\begin{aligned} G_x = \frac{\partial \phi_B}{\partial x} &= \frac{\partial}{\partial x} \left[\tan^{-1} \left(\frac{Ax}{a^2}\right)\right] = \frac{A/a^2}{1 + (Ax/a^2)^2} \\ &= \left(\frac{1}{a}\right) \frac{A/a}{1 + (A/a)^2 (x/a)^2} \end{aligned} \tag{10}$$

where (A/a) is the normalized degree of twist, and (x/a) the normalized distance along the encoding axis. This (x/a) factor indicates a non-linearity in the gradient, i.e. the gradient strength is a function of position along the encoding direction. The overall factor of $(1/a)$ indicates that for a given coil geometry, the phase gradient strength is inversely proportional to coil size, which is indeed an expected behaviour for any design of a phase gradient coil. As a general rule, a smaller coil will have both a shorter pulse length and a stronger gradient.

From the above equations, the magnitude of the B_1 field is calculated from the orthogonal sum of uniform axial and quadratic lateral components:

$$\begin{aligned} |B_1| &= \sqrt{B_y^2 + B_z^2} = \sqrt{\left(-\mu_0 \frac{I}{h} \frac{Ax}{a^2}\right)^2 + \left(\mu_0 \frac{I}{h}\right)^2} \\ &= \mu_0 \frac{I}{h} \sqrt{\left(\frac{Ax}{a^2}\right)^2 + 1} \end{aligned} \tag{11}$$

These analytical solutions for phase, phase gradient and field strength (Eqs. (10) and (11)) for the ideal infinite twisted coil are illustrated in Fig. 3, for a range of turn modulations. The figure illustrates that as the turn modulation is increased, the phase gradient increases, but the $|B_1|$ uniformity decreases, and the phase gradient linearity decreases. The choice of a modulation amplitude therefore involves a design trade-off between these three performance measures. For brevity we will refer to coils with modulated turns as 'twisted solenoids', with the word 'twisted' being synonymous with 'wound using modulated turns'.

In summary, the magnitude of the B_1 field varies in the x direction only, and so is uniform over any horizontal plane. Over the central horizontal $x = 0$ plane, the magnitude of the field is unaffected by the coil twist and is given by: $|B_1| = \mu_0 I/h$. The phase of the B_1 field similarly only varies in the vertical direction, so again the B_1 phase is constant over any horizontal plane. Over the central horizontal $x = 0$ plane the direction of the B_1 field is purely axial, as for a conventional solenoid. For a long twisted solenoid, since the field pattern varies as a function of x only, the field pattern over all transaxial planes are identical.

2.2.4. Generation of different phase gradients by coil rotation

The generation of phase gradient G_x has been discussed, assuming winding shift $\psi = 0$. However, with appropriate values of winding shift, other phase gradients such as $-G_x, G_y$ and $-G_y$ can also be created. Examining Eq. (7), a reversed B_y field is generated when $\psi = \pi$ because $\cos(\theta + \pi) = -\cos(\theta)$, resulting in the generation of the opposite phase gradient $-G_x$ using Eq. (10).

The creation of a phase gradient along y axis G_y is achieved as follows. For a winding shift of $(\psi = 3\pi/2)$, using trig identities and $y = \rho\sin\theta$, Eq. (7) simplifies to:

$$B_y = -\mu_0 \frac{I}{h} \frac{A\rho}{a^2} \cos(\theta + 3\pi/2) = -\mu_0 \frac{I}{h} \frac{Ay}{a^2} \tag{12}$$

and the B_1 phase is:

$$\phi_B = \tan^{-1} \frac{-B_y}{B_z} = \tan^{-1} \left(\frac{Ay}{a^2}\right) \tag{13}$$

Now the phase only depends upon the y coordinate, so there is no gradient along x axis, i.e. $G_x = 0$. The phase gradient in the y-direction can be expressed as:

$$\begin{aligned} G_y = \frac{\partial \phi_B}{\partial y} &= \frac{\partial}{\partial y} \left[\tan^{-1} \left(\frac{Ay}{a^2}\right)\right] = \frac{A/a^2}{1 + (Ay/a^2)^2} \\ &= \left(\frac{1}{a}\right) \frac{A/a}{1 + (A/a)^2 (y/a)^2} \end{aligned} \tag{14}$$

This formula is identical to Eq. (10), with only x substituted by y. Similarly, we can prove that winding shift $(\psi = \pi/2)$ is capable of producing $-G_y$ phase gradient along y axis. These gradient directions and winding shifts are summarized in Table 2.

3. Practical coil design

In this section we describe the design of a practical RF transmit coil, based on the twisted solenoid geometry, for the purpose of

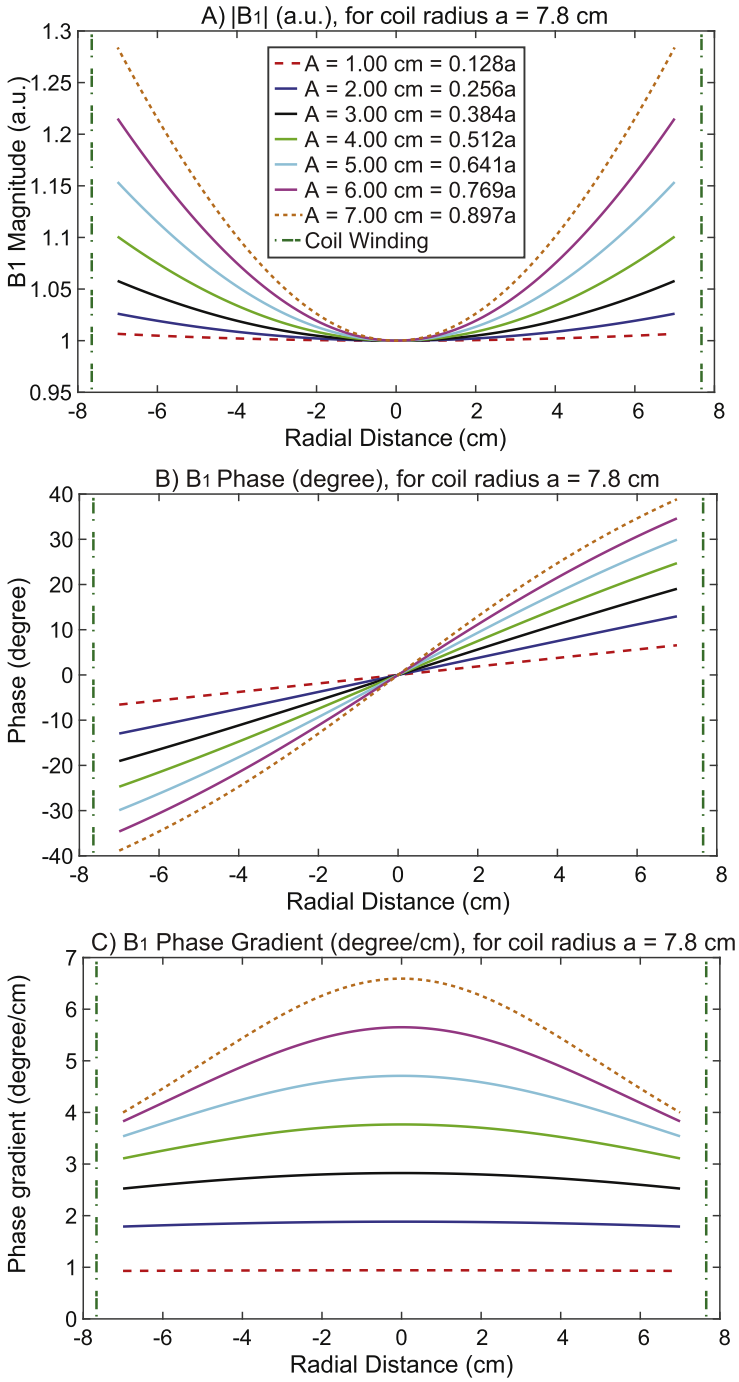

Fig. 3. Field plots for analytical solution for ideal infinite twisted coil, for a range of turn modulations: (A = 1 cm, 2 cm,. . ., 7 cm) (A) B_1 magnitude; (B) B_1 phase, ϕ_B; (C) Phase gradient, G_x. The radius of the coil winding is indicated by vertical green dotted lines. These plots show that as the modulation increases, the phase gradient strength increases, however the B_1 magnitude uniformity worsens, and the linearity of the phase gradient also deteriorates. Coil design therefore involves a trade-off between these parameters. (For interpretation of the references to color in this figure legend, the reader is referred to the web version of this article.)

Table 2
Winding shifts and coil rotation for 4 orthogonal phase gradient directions. Other transverse gradient directions are also possible (not shown.)

Phase gradient	Winding shift (ψ)	Coil rotation
$+G_x$	0°	0°
$-G_x$	180°	90°
$+G_y$	270°	135°
$-G_y$	90°	45°

TRASE imaging. The optimum design of conventional solenoidal transmit/ receive coils at lower field has been studied by Blasiak et al. [19]. For the design of a 8.2 MHz solenoidal head coil (inner diameter (I.D.) 28 cm, length 28 cm), the authors reported an optimum balance between B_1 uniformity and SNR was achieved by a 9-turn coil using 1/4 inch outer diameter (O.D.) copper tubing. This design followed the rule of thumb that turn-spacing should be at least three times the conductor diameter, due to the proximity effect.

For the design of TRASE transmit coils the priorities are different from those of Blasiak et al. since, although coil efficiency remains a design consideration, the coil field pattern produced has higher priority, because it determines the spatial encoding. Also, although, for convenience, the TRASE coil may often be used as receiver, in an optimized design a dedicated receive coil or array should be used, hence receiver performance of the twisted solenoid becomes a secondary consideration. In general, the tight specifications on the transmit field pattern of the coil tends to favour larger coils, whereas high sensitivity favours smaller coils.

3.1. Design aims & procedure

3.1.1. General design aims

The general design aim for the twisted solenoid is to maximize the phase gradient strength over a defined imaging volume, subject to constraints on B_1 homogeneity, coil efficiency and coil geometry. Also note that the geometry limits the maximum phase gradient strength, as the modulation A approaches radius a. Phase gradient linearity was not explicitly used as a criterion because while the other parameters affect the execution of the experiment, nonlinearity only affects the image geometry, which can be corrected for post acquisition. Also, given our geometric constraints, the phase gradient linearity is closely correlated with the other measures (see Fig. 3). The maximization of coil efficiency is favoured by high B_1 strength (i.e. closer wound turns) and high coil Q. In this study decoupling between the two transmit coils was achieved geometrically, which avoids the issue of potential Q degradation due to losses in PIN diode switches. Also, we have specified a fixed winding shift, $\psi = 0$ and a fixed coil radius (see below), so the design task is reduced to finding optimum values for the following coil geometric parameters:

- A - modulation amplitude
- h - turn advance
- N - number of turns

Total coil length is not an independent parameter, but a maximum acceptable coil length is specified.

3.1.2. Specific design target and constraints

To suit the magnet system used in this study, the coil design was based on a 6-inch O.D. acrylic cylindrical former, which corresponds to a coil turn radius of a = 78 mm. The maximum acceptable coil length along the z axis was specified as 450 mm. The conductor was wound with solid 12 AWG hookup wire (Digikey). Since the ultimate aim is to wind four such coils in a single cylindrical structure, this relatively narrow conductor diameter is beneficial, despite the potential for slightly increased ohmic losses. The design was also constrained to be an integer number of evenly-spaced turns, each of the modulated twisted geometry, as already described. No attempt was made to modify the coil design to compensate for the finite length of the coil, although there is scope to investigate this in future studies. The cylindrical target imaging volume was specified as follows:

1. A diameter of 110 mm, equal to 70% of the diameter of the cylindrical former (110 mm = 0.7 × 156 mm).
2. A length of 100 mm along the z-axis (axial direction)

It is worth commenting that this is a reasonable, yet arbitrary, choice of imaging volume, and that different target volumes would yield different coil designs. In particular, specifying a smaller target diameter (as percentage of coil diameter) would permit a larger modulation (i.e. more twist) resulting in a stronger phase gradient.

3.1.3. Design procedure

The design strategy adopted was to search through a large number of field simulations corresponding to candidate coil geometries, and to select an optimum design from ranking and scoring the field patterns.

In this work the B_1 field created by each coil winding pattern was calculated with Biot-Savart simulations using the BSMag MATLAB package, where the wire pattern was segmented into 720 straight-line current segments per turn[20]. For our relatively low frequency of interest (9.28 MHz), these quasi-static Biot-Savart simulations provide a good approximation of the magnetic field produced by coil currents, provided that the RF current phase does not vary significantly throughout the circuit. The rule of thumb is that current paths should be $L < \lambda/20$, which corresponds to around $L = 1.6$ m (free-space). In construction, capacitors were used to break up the long wire to mitigate wavelength effects [21].

3.1.4. Search procedure: parameters

The B_1 field was simulated using the following parameter search ranges:

- Depth of modulation, A(cm): 1.0 cm …10.0 cm, (in $\Delta A = 0.5$ cm increments)
- Turn spacing, h(cm) = 1.0 cm …10.0 cm, (in 0.5 cm increments)
- Number of turns, N = 2, 3, 4, 5, 6, 7, 8, 9, 10

Select/Reject Criteria:

- The acceptance criterion for field uniformity was $|B_1|/|B_1 min| < 1.25$ over the imaging target volume, corresponding to a flip angle range of 160–200°.
- The acceptance criterion for mean phase gradient strength was $G_x \geqslant 5.0$ deg/cm

Ranking Criteria: Coil winding patterns that passed the first test are shown in Table 3. These 9 designs were then ranked by defining a coil efficiency metric (η_{coil}) as the product of median B_1 field strength and mean phase gradient such that $\eta_{coil} = B_{1med} G_x$.

3.1.5. Biot-Savart simulation results

The top ranking design (labelled #1), a 10-turn coil with 3 cm turn advance and a 5.5 cm modulation, is shown in Figs. 4 and 5, and was selected for construction. As expected, the numerical results duplicated the general features of the analytical current sheet solution, but differ due to both the finite coil length and the finite turn spacing.

4. Experimental methods

4.1. Coil construction

Twisted Solenoid: A 10-turn 78 mm radius twisted solenoid was wound from 12 AWG solid hookup wire, upon a 6 inch (152 mm) O.D. cylindrical acrylic former. The twisted solenoid wire path is shown in Fig. 4, where coil geometry parameter values are modulation A = 55 mm, winding increment (turn advance) h = 30 mm. A schematic and photograph of the constructed coil are shown in Fig. 6.

Saddle Coil: To demonstrate one-dimensional TRASE imaging encoding, a second coil is needed with a different phase gradient. One option is to use a conventional RF coil which provides zero phase gradient, here an orthogonal saddle coil was constructed [21]. Using a 5 inch (127 mm) O.D. cylindrical acrylic former, the saddle coil was constructed with a length-to-diameter ratio of 2 and circular arcs of 120°. This particular geometry has been proved to be an optimal geometry for generating a uniform magnetic B_1 field, because no second order central field derivatives is generated

Table 3
Simulation results of different twisted solenoid coil geometries.

#	Modulation A (cm)	Turn advance h (cm)	Turns N (count)	Mean B_1 phase gradient G_x (deg/cm)	B_1 field strength per unit current at origin B_1(0,0,0) (uT)	Median B_1 field strength per unit current within imaging volume B_{1med} (uT)	Wire length L (m)	Coil efficiency η_{coil} (uT· deg/cm)
1	5.5	3	10	5.27	36.61	37.05	6.81	195.39
2	6	3.5	10	5.51	32.44	32.88	7.10	181.14
3	5	3	9	4.98	35.67	36.03	5.88	179.48
4	5.5	3.5	10	5.14	32.51	32.88	6.81	168.93
5	5.5	3.5	9	5.23	31.78	32.16	6.13	168.14
6	5.5	4	9	5.12	28.61	28.92	6.13	148.02
7	5.5	4	8	5.22	27.92	28.24	5.45	147.33
8	6	4.5	8	5.49	25.39	25.71	5.69	141.14
9	5.5	4.5	8	5.12	25.44	25.70	5.45	131.56

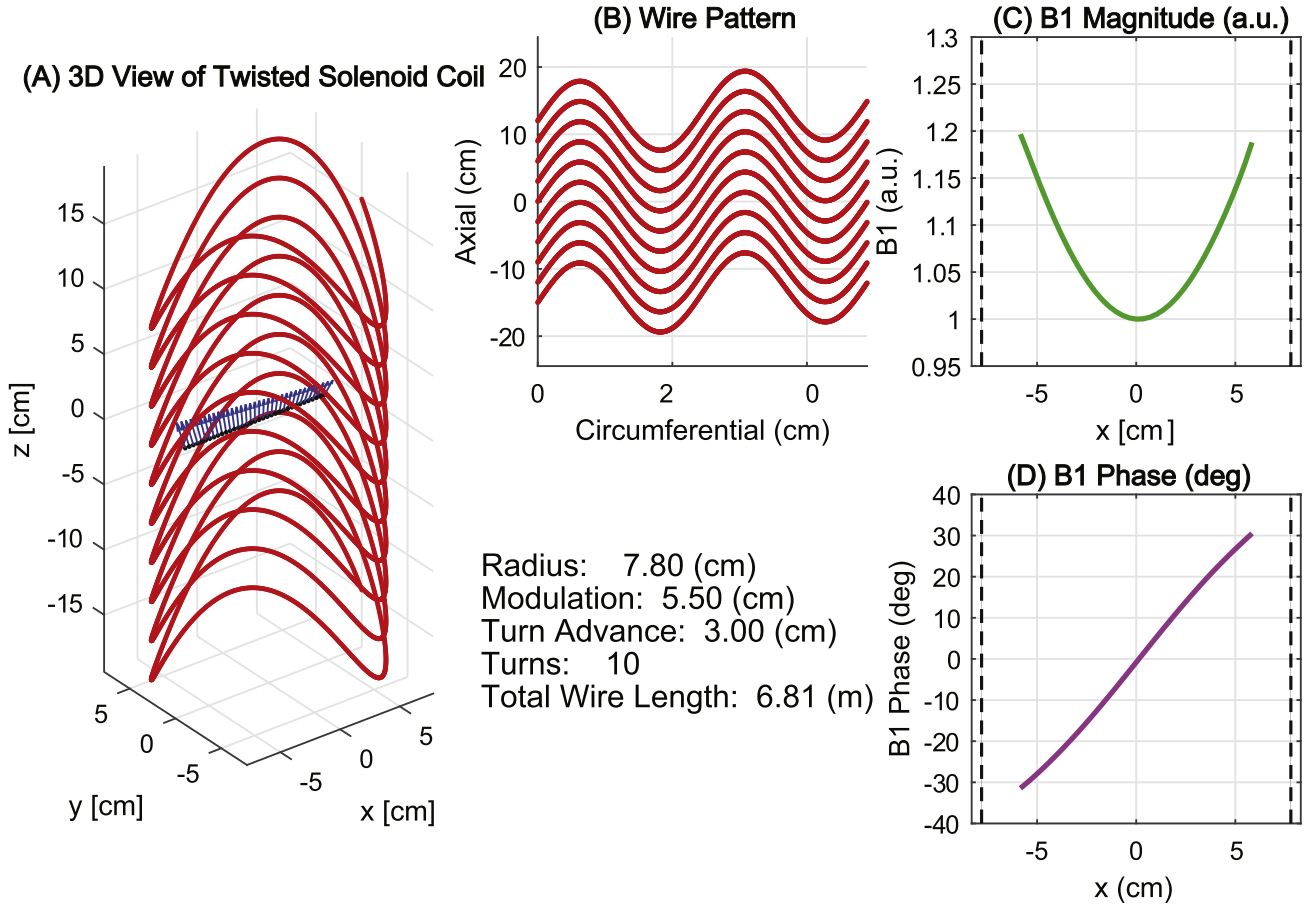

Fig. 4. Field plots for optimum twisted solenoid coil using Biot-Savart's Law calculation (A) 3D view of coil, showing field measurement points; (B) Unrolled view of wire winding pattern; (C) B_1 magnitude along x axis (D) B_1 phase along x axis. Position of coil windings is indicated by vertical dotted lines. Geometric parameters are shown in the figure.

in any direction [22]. The saddle coil has an extra wire loop of diameter of 11 cm at one end, which allowed coil decoupling to be achieved purely geometrically, simplifying the experimental arrangement, and allowing twisted coil efficiency to be evaluated without potential losses from PIN diode circuitry. The saddle coil was configured with a T/R switch so that it can operate as either transmitter and receiver. The coil circuit schematics and photographs of the constructed coils are also shown in Fig. 6.

4.2. MRI equipment

MRI experiments were performed on a 9.28 MHz 4-poster permanent magnet with a vertical B_0 field, equipped with conventional B_0 imaging gradients with opening between planar gradient coils of 21.5 cm. The B_0 gradients were used for shimming only. The MRI system was controlled by an NRC TMX research console [23], equipped with a single transmit channel and two receive channels. The single transmit channel was configured to drive two RFPAs in alternation. Firstly, a 50:50 RF power splitter (Minicircuits) was used to divide the RF drive signal. Secondly, the RF gating signal was processed by an Arduino single board computer (Mega 2560) to generate two RFPA enable (gating) signals. Following the detection of a dummy signal from the console, controlled by a user-defined program, the board generates two digital gating signals (+5 V) to alternately enable the RFPAs. The two independent RF power amplifiers used to drive the two coils were as follows: the twisted coil was driven by an AN8110 RF Amplifier (Analogic Corp MA, USA), and the saddle coil by a Tomco model

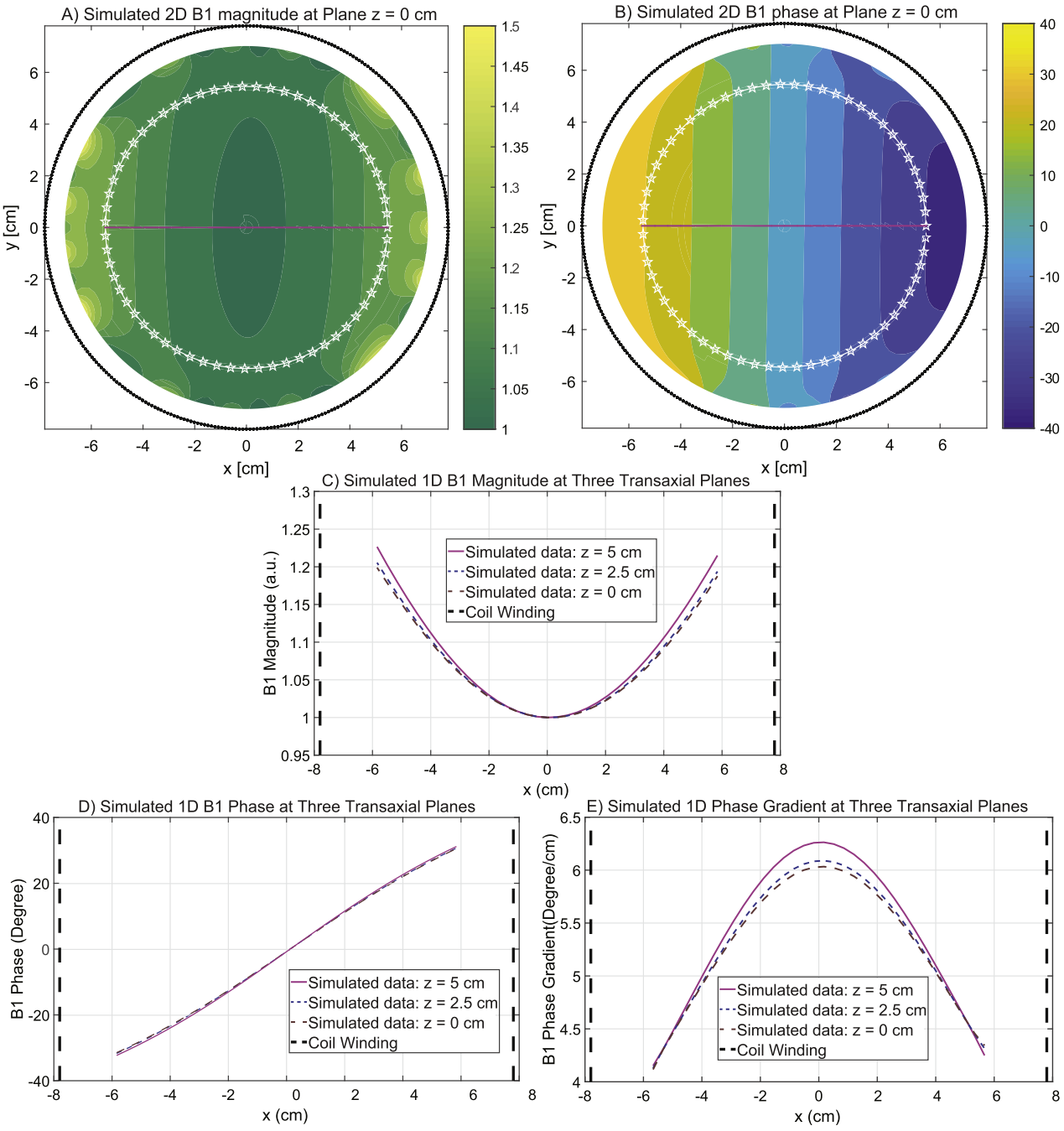

Fig. 5. B_1 field plots using Biot-Savart simulations for the optimum coil design (a = 78 mm, A = 55 mm, h = 30 mm, N = 10). 2D simulated B_1 field at plane z = 0 cm, showing: (A) 2D B_1 magnitude map; (B) 2D B_1 phase map. The coil winding and target imaging volume are depicted as black dotted line and white pentagram line, respectively. The horizontal magenta line indicates the position of the 1D profiles. For three different transaxial planes (z = 0 cm, 2.5 cm, and 5.0 cm) 1D profile lines are shown for: (C) 1D B_1 magnitude; (D) 1D B_1 phase; (E) 1D B_1 phase gradient. $|B_1|$ lies in between 1.00 and 1.25 within the target imaging volume, corresponding to refocusing flip angle of 160° at the center of coil, and 200° approaching the coil windings. The phase gradient is strongest centrally, decreasing in strength radially. For larger z offsets, the phase gradient is slightly stronger, while the B_1 uniformity is slightly worse, which is a commonly seen trade-off [2].

BT00500 RF amplifier (Tomco Technologies, Australia). The T/R switch used was actively switched [24]. A low noise (noise figure = 1.2 dB), 50 Ω, high gain (50 dB) pre-amplifier (AU 1448-8064) was used to amplify the received signal (Miteq, NY, USA).

4.3. Coil Q RF power measurement procedures

For bench RF measurements, RF S-parameters and coil Q were measured using an Agilent Technologies E5061A network analyzer. RF voltages were measured using an oscilloscope (Model MDO4054B-3 Tektronix). Using two small search loops connected to the 50Ω network analyzer, coil Q was measured under two conditions: (1) without load ($Q_{unloaded}$) , and (2) with human forearm positioned in the center of the coil (Q_{loaded}). A cylindrical phantom, of diameter of 47 mm and length 80 mm, was used to mimic the forearm loading by adding NaCl to tap water until the same Q_{loaded} was reached.

RF power was measured in the magnet with the solenoid coil being connected to the AN8110 RF amplifier, in series with an active T/R switch. Positioned in the magnet with loaded phantom,

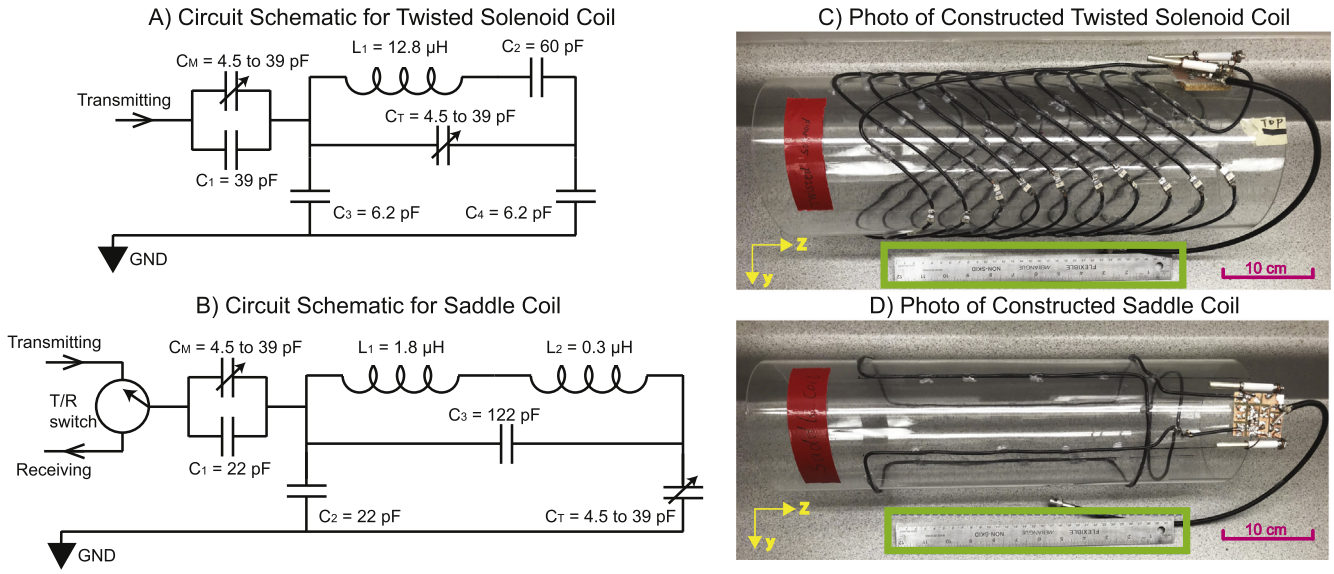

Fig. 6. Photos of constructed coils and corresponding circuit schematics. (A) Balanced circuit schematic for twisted solenoid coil. C_2 represents the value of ten capacitors in series with the long wire to mitigate wavelength effects; (B) Balanced circuit schematic for saddle coil. L_2 denotes the extra circular wire loop on the coil right hand side, which can be adjusted for geometrical decoupling. Active T/R switch is also depicted in the schematic, showing that in TRASE experiment saddle coil is used as both transmitter and receiver; (C) Photograph of constructed twisted solenoid coil; (D) Photograph of constructed saddle coil. The saddle coil is at smaller size (O.D. of 5 inch), and nests inside the twisted solenoid coil (O.D. of 6 inch).

the twisted solenoid coil was tuned and matched, as indicated by reflection coefficient S_{11} measurement at the resonant frequency. The RF power required by the coil for a 180° flip angle (for a given pulse length) was determined from NMR measurements by first adjusting the power using a spin-echo sequence, maximizing the echo amplitude. The forward and reflected power in this condition was then determined from a calibrated directional coupler inserted into the RF output path. For verification, the RF output power was also calculated by measurement of the RF input signal to the RFPA and using the known gain of the amplifier at the Larmor frequency. This calculated output power is expected to match the sum of the forward and reflected power measurements.

4.4. Field profile measurement procedures

To assess the amplitude and phase of the generated B_1 transmit fields, bench tests were performed with a pick-up coil to measure the two field components B_y and B_z within the specified imaging volume. The shielded and balanced pick-up coil was constructed from flexible co-axial cable [24], and formed an ellipse with major and minor axis 20 mm and 10 mm, respectively. Five different transaxial planes (z = −50 mm, −25 mm, 0 mm, 25 mm, 50 mm) were evaluated. In each z plane the field along three lines (y = −15 mm, 0 mm, +15 mm) were measured at 11 different x positions varying between −52 mm to +45 mm, with 5 repetitions. Throughout the entire procedure, the twisted solenoid coil was positioned on a 10 cm thick foam block without loading, inside of which the pick-up coil was positioned perpendicular to the orientation of each evaluated field component. With a network analyzer, the S_{12} measurement mode was used to detect the B_y and B_z magnitude (linear scaling), and the corresponding phase information (to detect field sign reversal).

4.4.1. Calculations and data fitting procedures

B_1 Magnitude and Phase: The B_1 magnitude and phase were calculated directly from the B_y and B_z measurements as $|B_1| = \sqrt{B_y^2 + B_z^2}$, and $\phi_B = \tan^{-1}(-B_y/B_z)$, both of which are plotted in Fig. 7. The error associated with each point in the figure was calculated using error propagation, where the errors of B_y and B_z were represented by standard deviation of five raw measurements.

B_1 Phase Gradient Methods: The B_1 phase gradient was not directly estimated (by differentiating the measured phase points) as this is known to be a noise-sensitive procedure. Instead, to appropriately evaluate the phase gradient, we used second-order polynomials (as suggested by the simulation results) to directly fit the raw B_y and B_z measurements, because both magnetic field components are expected to be smooth functions. Next, using these two fitted field curves, the phase gradient was evaluated at 20 points evenly-spaced points on the x-axis:

$$G_x = \frac{\Delta \tan^{-1}(-B_y/B_z)}{\Delta x_i},$$

where Δx_i is defined as the chosen x interval. In the fitting process ΔB_y and ΔB_z (the estimates of the standard deviation of the error in predicting B_1 magnetic fields at x) were calculated using the MATLAB *polyval* function. These estimated errors were propagated to evaluate the accuracy of the evaluated phase gradient curves.

5. Experimental results

5.1. Coil Q and power results

Unloaded and loaded coil Qs was measured as $Q_{unloaded} = 390$ and $Q_{loaded} = 285$, respectively. The Q damping-ratio was $r = Q_{loaded}/Q_{unloaded} = 0.73$. Within the magnet, with the NaCl doped phantom in position, the twisted solenoid coil was tuned to the resonant frequency f = 9.278 MHz, and matched to 50 Ω with $S_{11} = -22$ dB. For a single spin echo experiment, with a 300 μs, 180° hard pulse, the monitor peak-to-peak voltages were measured as $P_{forward}$ = 45.97 W, and $P_{reflected}$ = 8.58 W. For additional verification, the actual amplifier RF input power P_{input} was also measured using the scope. After amplification of +64 dB, the total output RF power generated from the amplifier was calculated as P_{total} = 55.49 W (see details in Table 4). The sum of $P_{forward}$ and $P_{reflected}$ 54.55 W agrees closely with this measurement. In conclusion, a power level at the coil of around 46 W is required to drive

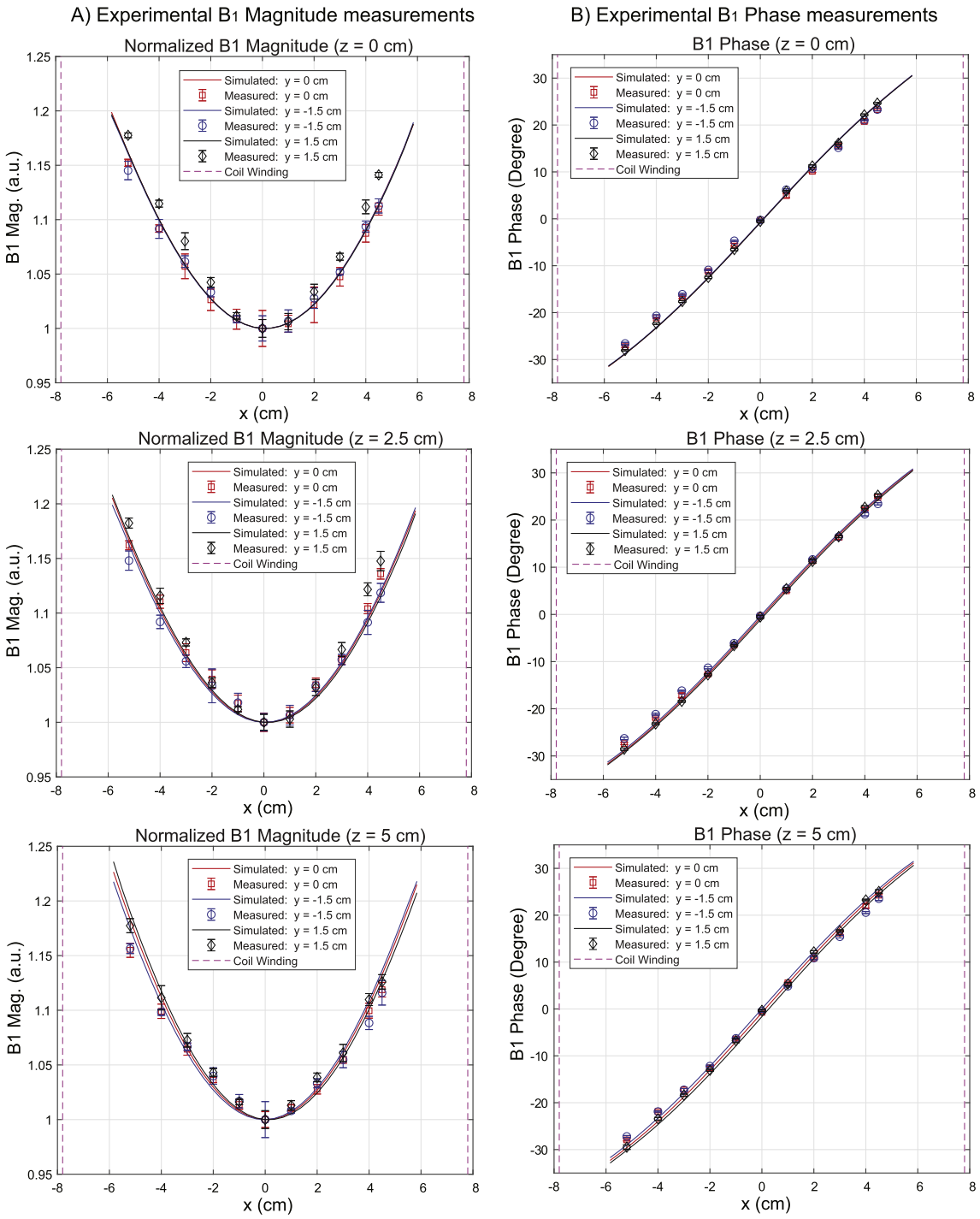

Fig. 7. Experimental and simulated results for B_1 magnitude and phase. (A) Comparison of simulated and measured B_1 magnitude along three different y lines on three transverse planes (z = 0 cm, 2.5 cm, 5.0 cm); (B) Comparison of simulated and measured B_1 phase for the same locations as in (A). The Biot-Savart simulated data are plotted in the figure as solid lines. The other two measured planes at $z = -2.5$ cm, -5.0 cm showed very similar results to these (not shown).

a 300 μs 180° hard pulse with a forearm-like phantom. Although the coil itself was well matched, the additional components between amplifier and coil (long (approx.) 5 m cable, T/R switch) may have contributed to the reflected power.

5.2. Coil field plot results

The measured coil field data including $|B_1|$, phase and phase gradient are shown in Figs. 7 and 8. The simulated data are also shown in each plot for comparison. Due to the relative large size of the pickup-coil (major and minor axes of 2 cm and 1 cm, respectively), it was impractical to measure the fields at the edges of the targeted imaging volume. Additionally, when measurements were made at $x \geqslant 3.0$ cm, a displacement of $y = 1.5$ cm was the furthest off-center point that could be evaluated due to the cylindrical geometry of the coil. Therefore for consistency between measurements, we restricted all measurements to $y \leqslant 1.5$ cm. Data are shown for planes at $z = 0$ cm, 2.5 cm and 5 cm in the figure. Similar measured B_1 magnitude and phase results for planes $z = -2.5$ cm and -5.0 cm are not shown. The deviation between simulations and measurements were evaluated by comparing measured points with the corresponding value on the simulated curve. Maximum

Table 4
RF power measurements for twisted solenoid coil. The peak-to-peak voltage shown is for a 300 μs, 180° pulse.

Signal	Power gain from measured channel to twisted solenoid coil	Peak-to-peak voltage scope (50Ω)	Peak power
Amplifier forward monitor	+40 dB	1.356 V	$P_{forward}$ = 45.97 W
Amplifier reflected monitor	+40 dB	0.586 V	$P_{reflected}$ = 8.58 W
Console input to RFPA	+64 dB	0.094 V	P_{total} = 55.49 W

deviations for B_1 magnitude, phase and phase gradient were 3.2%, 3.4%, and 8.3%, respectively.

5.3. TRASE imaging results

The pairing of the twisted solenoid and the saddle coil enabled a one-dimensional TRASE encoding to be conducted. The twisted solenoid coil was designed for transmission only, whereas the saddle coil was responsible for both transmission and receiving, controlled by an active T/R switch. A TRASE imaging experiment was performed using a bottle phantom of diameter of 4.7 cm,

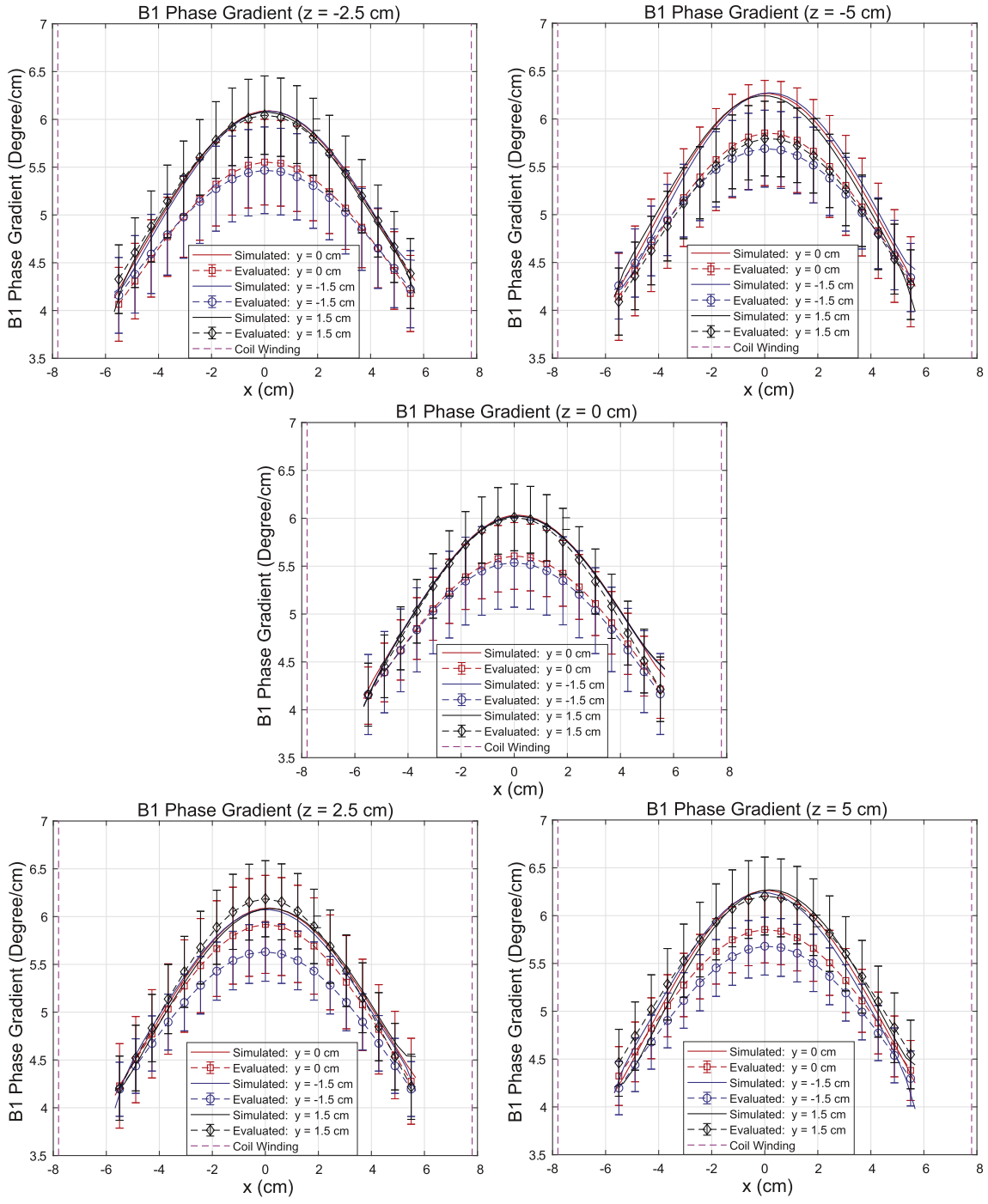

Fig. 8. Bench measurement of B_1 phase gradient and simulation results. The Biot-Savart simulated and the measured B_1 phase gradients were both plotted for five z planes (z = −5.0 cm, −2.5 cm, 0 cm, +2.5 cm, +5.0 cm), and three y lines (y = −1.5 cm, 0 cm, 1.5 cm) on each plane. The measured phase gradient strength is equal to or lower than the simulation in all cases.

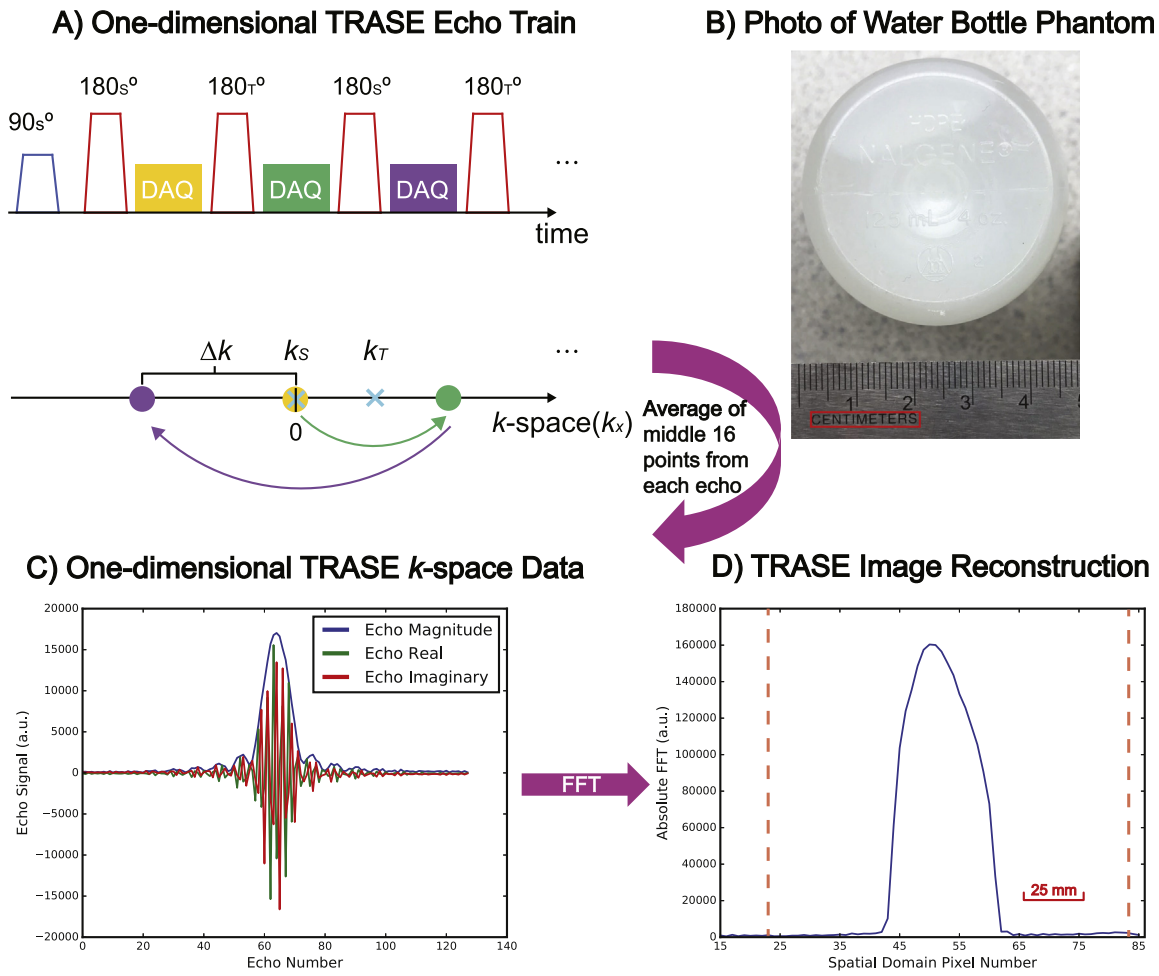

Fig. 9. One-dimensional TRASE experiment (A) 1D TRASE pulse sequence consisted of two groups of alternating refocusing pulses 180°_{S} and 180°_{T}, where *S* and *T* represent saddle and twisted solenoid coil, respectively. DAQ denotes the sampling of each echo between two adjacent 180° pulses. In *k*-space, each refocusing pulse activates a jump about the corresponding coil *k*-space origin (k_S and k_T). Note that the saddle coil produces a uniform B_1 field, i.e. zero phase gradient, hence the coil origin coincides with the origin of *k*-space. This pair of coils is sufficient to demonstrate the twisted solenoid coil's encoding capability. However, more efficient TRASE encoding could be achieved by using two twisted solenoid coils generating opposite phase gradients, which would double the *k*-space sampling interval Δk, providing higher resolution, for the same *ETL*. (B) Imaged phantom filled with tap water. This cylindrical phantom has a diameter of 4.7 cm. The sequence parameters were NA = 1, echo spacing 2000 μs, pulse duration 300 μs for both excitation and refocusing pulses, readout 32 points at 100 kHz bandwidth, delays of 50 μs both before and after the refocusing pulses. (C) Experimental acquired echoes along *x* axis. The echoes were re-ordered for display because the actual acquired echoes were in an order of $+k, -k, +k, \ldots$, caused by the jump pattern in *k*-space. (D) 1D TRASE image obtained from Fourier transform of acquired echoes in C). Based upon measurements, the pixel width was 2.47 mm while the FOV was 322 mm which covered the entire coil space. The coil position was also depicted here, indicated by dotted lines.

length of 8.0 cm, containing tap water. At the resonant frequency *f* = 9.278 MHz, with phantom and both coils in position in the magnet, the scattering matrix was measured as S_{11} (saddle coil) = −32 dB, S_{22} (twisted solenoid coil) = −33 dB, S_{12} (geometrical decoupling) = −31 dB. The one-dimensional TRASE sequence used 300 μs hard pulses for both excitation (90° pulse) and refocusing (180° pulses), with echo spacing time 2000 μs, *ETL* = 128, and number of averages, NA = 1. For each spin echo, 32 points were sampled at a receiver bandwidth of 100 kHz, using the mean of the middle 16 points to represent a single data point in *k*-space. The applied sequence, phantom and obtained 1-D TRASE profile are shown in Fig. 9. The width of 1D phantom image profile was represented by 19 pixels, corresponding to a mean pixel size of 2.47 mm/pixel and a mean phase gradient of G_x = 5.69 deg/cm.

6. Discussion

The B_1 magnitude measurements (Fig. 7) agree closely with the Biot-Savart simulations, with no observable trend of deviation (largest deviation 3.2%). The phase plots also show close agreement (largest deviation of 3.4%), but with some discernible systematic deviation, as shown more clearly in the phase gradient plots, as discussed next. The measured phase gradient and the corresponding simulation results are shown in Fig. 8. The simulated and measured data show good overall agreement with the strongest gradient strength appearing in the middle and decreasing radially. The largest point-to-point deviation is 8.3%. The B_1 phase plots in Fig. 8 show that the measured B_1 phase gradients are either equal to or weaker than the simulations, but are generally within the error bars. For 4 out of 5 *z* planes ($z = -5$ cm being the exception), the y = 1.5 cm measured curve (black) showed the best match to the simulated curve. The measured data on these 4 *z*-planes presented similar trends for three *y* lines, with the phase gradient higher for y = 1.5 cm (black) than for $y = -1.5$ cm (blue). These discrepancies in the *y*-direction may have been caused by the straight return wire (see Fig. 6), which was not included in the simulations, and introduces an asymmetry in *y*-direction for the magnetic fields. Other possible sources of discrepancy and measurement inaccuracy include imperfections in coil construction, the finite size of the pick-up coil, and the line of additional capacitors on one side of the coil.

An important aim of this work is to reduce the overall length of the echo train to reduce T_2 resolution loss. By use of RF amplifiers allowing higher duty cycle, the 256 ms train duration used here could be significantly reduced (200 μs with two amplifiers, each operating at 25% duty cycle, yields 0.2 ms × 128 = 64 ms). To avoid resolution loss, as a rule of thumb, the echo train should be no longer than 1.2 times the shortest T_2.

Due to Specific Absorption Rate (SAR) limitations of higher fields, TRASE is better suited to lower field MRI. At 0.2 T calculations (for head coil) show that 2900 pulses per second, each of 200 μs duration, would remain within SAR limits. At this rate 128 × 128 *k*-space points could be acquired in under 6 s. Although this is an approximate and raw calculation ignoring sequence design details, the data rate provided by TRASE is clearly practical for anatomical imaging at 0.2 T. However since SAR increases with the square of the field strength, the permissible pulse rate falls rapidly for higher fields, and the use of many long TRASE echo trains becomes progressively more restrictive. For full TRASE encoding, fields in the range of 0.3 T to 0.4 T or lower are more flexible. However since $(1.5/0.2)^2 = 56$, the SAR at 1.5T is 56 times higher than at 0.2 T, illustrating that the high field MRI regime is not hospitable to TRASE encoding.

For a simple Fourier transform image reconstruction, the non-uniform magnitudes of the phase gradient will distort the resulting image due to variable spatial resolution, with the center of coil producing the highest resolution. However, since the variation of the phase gradient is known, based on the coil geometry, the image can be accurately reconstructed using other algorithms such as regularized least squares [14]. For future variants, it would be useful to study the design of the solenoid end turns to better control the coil length, while maintaining overall coil performance.

We conclude that Biot-Savart simulation is a good indicator for phase gradient generated by twisted solenoid coil, at our low operating frequency, although we cannot exclude the possibility of deviation between the measured and simulated data based on the limits of the quasi-static approximation. Future full wave simulations and more precise control of coil construction may reduce this deviation.

The 1D TRASE imaging experiment resulted in a mean spatial resolution of 2.47 mm/pixel, corresponding to a measured mean phase gradient of G_x = 5.69 deg/cm, over the 4.7 cm diameter of the bottle phantom. This is in close agreement with both the mean phase gradient from simulation of 5.79 deg/cm, (Fig. 3), and also with bench measurements of 5.58 deg/cm (Fig. 8) over the same region. These correspond to deviations of 1.8% and 2.0%, respectively.

In this work, the refocusing pulse applied in the measurement was 300 μs, which required a peak RF power at the coil of 46 W. Although it is difficult to make a direct comparison with previously reported results for other coil geometries because of variations in geometry, construction and RF power, the solenoid is an inherently power-efficient and space-efficient design, putting clinical resolution imaging with practical RF power levels and compact magnets within reach.

7. Conclusions

The main purpose of this paper has been to introduce and evaluate the twisted-solenoid coil relative to previously published designs of TRASE phase gradient encoding coil, most notably the rectangular Helmholtz-Maxwell coil array [2]. The twisted solenoid coil has a large number of attractive characteristics, inherited from the venerable solenoid coil, including the efficient generation of a large cylindrical volume of uniform B_1 field. Geometrically, the cylindrical twisted-solenoid coil is compact, offering an open unobstructed aperture, a large fraction being usable as the imaging volume. The cylindrical outer shape is particularly advantageous for cylindrical Halbach-style permanent magnets, relative to the rectangular Helmholtz-Maxwell design.

For the twisted-solenoid design, since the entire phase gradient field is produced by a single current path, the phase gradient strength and $|B_1|$ field homogeneity is reliably known and not subject to experimental perturbation. In contrast, the Helmholtz-Maxwell designs require current balancing between parallel elements, which must be simultaneously resonant, while remaining decoupled. However, by control of the current ratio the Helmholtz-Maxwell designs do offer the possibility of varying the gradient strength (albeit also the homogeneity), which might be useful in some applications.

The twisted solenoid phase gradient direction can be set to any transverse direction by rotating the coil about the cylindrical axis, remembering that a 1 degree rotation of the coil rotates the gradient direction by 2 degrees. Therefore the four phase gradient fields necessary for 2D encoding $(+G_x, -G_x, +G_y, -G_y)$ could be produced by a set of four concentric cylindrical twisted coils, each oriented at different rotation angles about the patient axis (z). This capability to rotate the gradient direction by simple coil rotation is not possessed by any other phase gradient coil design. Practical implementation of a multi-coil gradient set would require isolation between elements, which can be achieved by the use of PIN diode switches [12] to disable inactive elements. The aim of future work is to combine a 4-coil twisted solenoid gradient set with a static B_0 gradient [4,25] for axial slice selection, to achieve full 2D-encoding multi-slice imaging entirely without the use of switched B_0 gradients.

Acknowledgements

Natural Sciences and Engineering Research Council of Canada, Grant/Award Number: RGPIN-2016-05183. We thank the two reviewers for their detailed comments.

Appendix A. Supplementary material

Supplementary data associated with this article can be found, in the online version, at https://doi.org/10.1016/j.jmr.2018.12.015.

References

[1] J.C. Sharp, S.B. King, MRI using radiofrequency magnetic field phase gradients, Magn. Reson. Med. 63 (2010) 151–161, https://doi.org/10.1002/mrm.22188.
[2] Q. Deng, S.B. King, V. Volotovskyy, B. Tomanek, J.C. Sharp, B1 transmit phase gradient coil for single-axis TRASE RF encoding, Magn. Reson. Imaging 31 (6) (2013) 891–899, https://doi.org/10.1016/j.mri.2013.03.017.
[3] J.C. Sharp, S.B. King, Q. Deng, V. Volotovskyy, B. Tomanek, High-resolution MRI encoding using radiofrequency phase gradients, NMR Biomed. 26 (11) (2013) 1602–1607, https://doi.org/10.1002/nbm.3023.
[4] J.P. Stockmann, C.Z. Cooley, B. Guerin, M.S. Rosen, L.L. Wald, Transmit array spatial encoding (TRASE) using broadband WURST pulses for RF spatial encoding in inhomogeneous b0 fields, J. Magn. Reson. 268 (2016) 36–48, https://doi.org/10.1016/j.jmr.2016.04.005.
[5] J. Bellec, C.-Y. Liu, S.B. King, A target field approach to the design of rf phase-gradient coils, Proc. Intl. Soc. Mag. Reson. Med. 19 (2011).
[6] D. Alsop, T. Connick, G. Mizsei, A spiral volume coil for improved rf field homogeneity at high static magnetic field strength, Magn. Reson. Med. 40 (1998) 49–54.
[7] Stephanie Yong, J.C. Sharp, The twisted solenoid rf phase gradient transmit coil for TRASE imaging, Proc. Intl. Soc. Mag. Reson. Med. 25 (2017), Honolulu, p. 4281.
[8] S. Ljunggren, A simple graphical representation of Fourier-based imaging methods, J. Magn. Reson. (1969) 54 (2) (1983) 338–343, https://doi.org/10.1016/0022-2364(83)90060-4. <http://login.ezproxy.library.ualberta.ca/login?url=http://search.ebscohost.com/login.aspx?direct=true&db=edselc&AN=edselc.2-52.0-0001313829&site=eds-live&scope=site>.
[9] D.B. Twieg, The k-trajectory formulation of the nmr imaging process with applications in analysis and synthesis of imaging methods, Med. Phys. 10 (5) (1983) 610–621, https://doi.org/10.1118/1.595331. <http://login.ezproxy.library.ualberta.ca/login?url=http://search.ebscohost.com/login.aspx?direct=true&db=edselc&AN=edselc.2-52.0-0020644027&site=eds-live&scope=site>.

[10] Q. Qin, Point spread functions of the T2 decay in k-space trajectories with long echo train, Magn. Reson. Imaging 30 (8) (2012) 1134–1142, https://doi.org/10.1016/j.mri.2012.04.017. <https://www.ncbi.nlm.nih.gov/pubmed/22817958>.
[11] W.D. Rooney, G. Johnson, X. Li, E.R. Cohen, S.G. Kim, K. Ugurbil, C.S. Springer Jr., Magnetic field and tissue dependencies of human brain longitudinal $1H_2O$ relaxation in vivo, Magn. Reson. Med. 57 (2) (2007) 308–318, https://doi.org/10.1002/mrm.21122. <https://www.ncbi.nlm.nih.gov/pubmed/17260370>.
[12] E. Der, V. Volotovskyy, H. Sun, B. Tomanek, J.C. Sharp, Design of a high power PIN-diode controlled switchable rf transmit array for TRASE rf imaging, Concepts Magn. Reson. Part B: Magn. Reson. Eng. doi:https://doi.org/10.1002/cmr.b.21365.
[13] S. Salajeghe, P. Babyn, G.E. Sarty, Composite pulses for RF phase encoded MRI: a simulation study, Magn. Reson. Imaging 36 (2017) 40–48, https://doi.org/10.1016/j.mri.2016.10.007.
[14] S. Salajeghe, P. Babyn, J.C. Sharp, G.E. Sarty, Least squares reconstruction of non-linear RF phase encoded MR data, Magn. Reson. Imaging 34 (7) (2016) 951–963, https://doi.org/10.1016/j.mri.2016.04.010.
[15] C. Goodzeit, M. Ball, R. Meinke, The double-helix dipole-a novel approach to accelerator magnet design, IEEE Trans. Appl. Supercond. 13 (2) (2003) 1365–1368, https://doi.org/10.1109/tasc.2003.812672.
[16] J. Alonso, A. Soleilhavoup, A. Wong, A. Guiga, D. Sakellariou, Double helix dipole design applied to magnetic resonance: a novel NMR coil, J. Magn. Reson. 235 (2013) 32–41, https://doi.org/10.1016/j.jmr.2013.07.004.
[17] R. Meinke, C. Goodzeit, M. Ball, Modulated double-helix quadrupole magnets, IEEE Trans. Appl. Supercond. 13 (2) (2003) 1369–1372, https://doi.org/10.1109/tasc.2003.812674.
[18] L. Queval, R. Gottkehaskamp, Analytical field calculation of modulated double helical coils, IEEE Trans. Appl. Supercond. 25 (6) (2015) 1–7, https://doi.org/10.1109/tasc.2015.2477377.
[19] B. Blasiak, V. Volotovskyy, C. Deng, B. Tomanek, An optimized solenoidal head radiofrequency coil for low-field magnetic resonance imaging, Magn. Reson. Imaging 27 (9) (2009) 1302–1308, https://doi.org/10.1016/j.mri.2009.05.018.
[20] L. Quéval, Bsmag toolbox user manual, tech. report, dept. elect. eng., university of applied sciences düsseldorf, germany, April 2015. Available: <http://www.lqueval.com> (accessed april. 07, 2015).
[21] D. Hoult, The NMR receiver: a description and analysis of design, Prog. Nucl. Magn. Reson. Spectrosc. 12 (1) (1978) 41–77, https://doi.org/10.1016/0079-6565(78)80002-8.
[22] D.M. Ginsberg, M.J. Melchner, Optimum geometry of saddle shaped coils for generating a uniform magnetic field, Rev. Sci. Instrum. 41 (1) (1970) 122–123, https://doi.org/10.1063/1.1684235.
[23] J.C. Sharp, D. Yin, R.H. Bernhardt, Q. Deng, A.E. Procca, R.L. Tyson, K. Lo, B. Tomanek, The integration of real and virtual magnetic resonance imaging experiments in a single instrument, Rev. Sci. Instrum. 80 (9) (2009) 093709, https://doi.org/10.1063/1.3202410.
[24] J. Mispelter, M. Lupu, A. Briguet, NMR Probeheads for Biophysical and Biomedical Experiments: Theoretical Principles and Practical Guidelines, Imperial College Press, 2015. <https://books.google.ca/books?id=u9vEbwAACAAJ> .
[25] G.E. Sarty, L. Vidarsson, Magnetic resonance imaging with rf encoding on curved natural slices, Magn. Reson. Imaging 46 (2018) 47–55, https://doi.org/10.1016/j.mri.2017.10.007. <https://www.ncbi.nlm.nih.gov/pubmed/29109052> .